Single-crystal growth and physical properties of the antiferromagnetic double perovskite Ba_2CoMoO_6

A. R. N. Hanna [1,*] M. M. Ferreira-Carvalho [2,3] S. H. Chen [2] C. F. Chang,[2] C. Y. Kuo,[4,5] A. T. M. N. Islam [1] R. Feyerherm [1] L. H. Tjeng [2] and B. Lake [1,6,†]

[1]*Helmholtz-Zentrum Berlin für Materialien und Energie GmbH, 14109 Berlin, Germany*
[2]*Max Planck Institute for Chemical Physics of Solids, Nöthnitzer Straße 40, 01187 Dresden, Germany*
[3]*Institute of Physics II, University of Cologne, Zülpicher Straße 77, 50937 Cologne, Germany*
[4]*Department of Electrophysics, National Yang Ming Chiao Tung University, 30010 Hsinchu, Taiwan*
[5]*National Synchrotron Radiation Research Center, 101 Hsin-Ann Road, 30076 Hsinchu, Taiwan*
[6]*Institut für Festkörperphysik, Technische Universität Berlin, Hardenbergstraße 36, 10623 Berlin, Germany*

(Received 16 March 2026; accepted 2 October 2026; published 27 October 2026)

This work presents a comprehensive investigation of the structural, magnetic, and electronic properties of the double perovskite Ba_2CoMoO_6 (BCMO). Single crystals were grown via floating-zone and Czochralski growth techniques and characterized using a set of complementary methods. X-ray diffraction analysis confirmed that BCMO crystallizes in a face-centered-cubic (fcc) structure with space group *Fm-3m*. Magnetic susceptibility measurements exhibit antiferromagnetic ordering below $T_N = 20.1(1)$ K. A spin-flop transition is observed at 26.5 kOe. Heat capacity measurements and entropy analysis are consistent with a $J_{eff} = 1/2$ ground state for Co^{2+} ions. X-ray absorption spectroscopy provided insight into the local electronic structure, revealing the spin-orbit and crystal-field effects. The cluster-model analysis yields a g factor of 4.36, consistent with a spin-orbit-entangled ground state. Surface photovoltage spectroscopy demonstrates a strong near-surface optical response with an onset near 1.5 eV and a pronounced feature at 2.65 eV, consistent with visible-range Co-O-Mo transitions in line with related Ba-based double perovskites, highlighting its potential for spintronic and energy-conversion applications.

DOI: 10.1103/6l9n-djww

I. INTRODUCTION

Double perovskite oxides with the general formula $A_2BB'O_6$ represent a versatile class of materials that exhibit diverse physical phenomena, including quantum magnetism, colossal magnetoresistance, and complex electronic behavior [1–5]. Their high-symmetry crystal structures—characterized by corner-sharing octahedra around alternating B and B' cations—provide an ideal platform for tuning properties via chemical substitution at the A, B, or B' sites [2,3,6–9]. When magnetic ions occupy the B site, they form a face-centered-cubic (fcc) sublattice, where competing exchange interactions and geometric constraints can stabilize a wide range of ground states from simple ferromagnets to frustrated antiferromagnets with substantial short-range correlations. In many Co-based systems, high-spin Co^{2+} in octahedral coordination realizes a $^4T_{1g}$ ground term with an effective orbital degree of freedom; spin-orbit coupling (λ) then splits this term into low-lying $J_{eff} = 1/2$, 3/2, and 5/2 multiplets on the scale of $|\lambda|$, giving rise to spin-orbit-entangled $J_{eff} = 1/2$ Kramers doublets that strongly influence magnetism and anisotropy [10–16].

Within this broader family, Ba-based double perovskites hosting Co together with $4d/5d$ cations have attracted considerable interest as model systems where geometrical frustration, spin-orbit coupling, and electronic correlations can be disentangled [6–9,17,18]. Ba_2CoMoO_6 (BCMO; space group *Fm-3m*) is a particularly appealing member: Co^{2+} and Mo^{6+} form rocksalt-ordered CoO_6 and MoO_6 octahedra within a Ba^{2+} framework, so that the Co ions occupy an undistorted fcc sublattice with well-defined Co-O-Mo-O-Co exchange pathways [see Fig. 1(a)], closely analogous to the isovalent compound Ba_2CoWO_6 [18–21]. In contrast to Sr_2FeMoO_6, commonly described by Fe^{3+} and Mo^{5+} valence states [22], stoichiometry and charge balance in BCMO point to a Co^{2+}/Mo^{6+} valence combination, and the Co^{2+} assignment can be tested directly by Co $L_{2,3}$-edge x-ray absorption spectroscopy (XAS) together with full-multiplet cluster calculations [10–15,23]. At the same time, antisite disorder between B and B' is known to strongly affect the magnetic and transport properties of double perovskites, as it suppresses the superlattice reflections associated with B-site order and disrupts the Co-O-Mo network; quantifying and minimizing such disorder is therefore essential for accessing the intrinsic properties, preferably in a single-crystal form.

*Contact author: Abanoub.Hanna@helmholtz-berlin.de
†Contact author: Bella.lake@helmholtz-berlin.de

Published by the American Physical Society under the terms of the Creative Commons Attribution 4.0 International license. Further distribution of this work must maintain attribution to the author(s) and the published article's title, journal citation, and DOI.

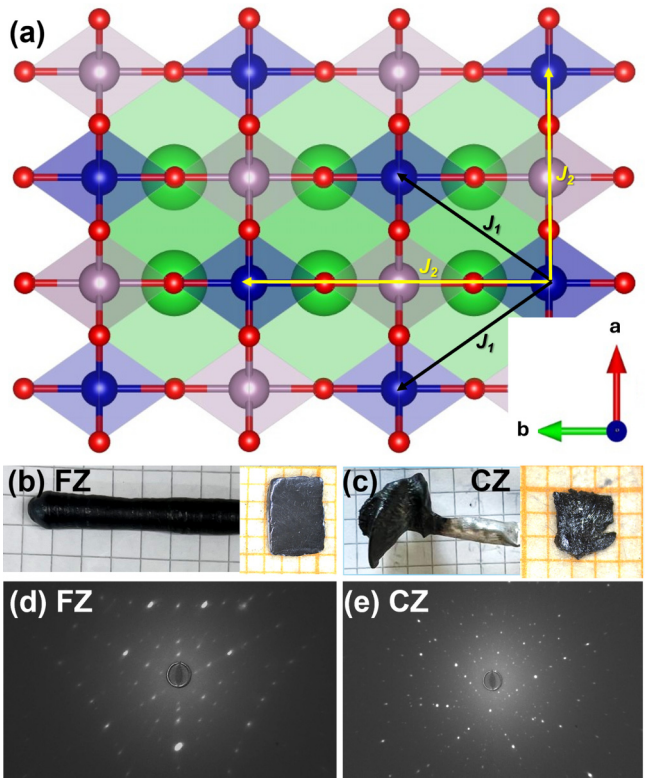


FIG. 1. (a) The crystal structure of Ba_2CoMoO_6 (BCMO) consists of Co^{2+} (blue), O^{2-} (red), Ba^{2+} (green), and Mo^{6+} (magenta) ions. The arrows represent the possible magnetic exchange interactions between Co^{2+} ions: nearest-neighbor interaction (J_1, black) and next-nearest-neighbor interaction (J_2, yellow) through superexchange between Co-O-Mo-O-Co. [(b), (c)] The BCMO crystals, grown using (b) the FZ technique and (c) the CZ technique. The insets to the right show the separated single crystals of dimensions $4 \times 3 \times 1$ mm^3 by FZ and $3 \times 2.7 \times 0.2$ mm^3 by CZ. [(d), (e)] Laue diffraction patterns of these crystals from FZ and CZ growths, showing [111] and [100] symmetry, respectively.

However, conventional solid-state synthesis of Ba_2CoMoO_6 typically yields polycrystalline samples containing impurity phases such as $BaMoO_4$ and CoO, with the former arising particularly under air annealing due to MoO_3 volatility. Previous work on BCMO has been restricted to powders and has not resolved the intrinsic magnetic anisotropy, the detailed $J_{\text{eff}} = 1/2$ level scheme, or the near-surface optoelectronic response. Single crystals are required to overcome grain-boundary and texture effects, to quantify antisite disorder from superlattice reflections, and to establish a reliable link between local electronic structure and bulk magnetism. In this work, we grow high-purity BCMO single crystals via floating-zone (FZ) and Czochralski (CZ) methods under argon atmosphere, and combine x-ray diffraction, magnetometry, heat capacity, surface photovoltage spectroscopy, Co $L_{2,3}$-edge XAS, and x-ray photoelectron spectroscopy (XPS) for Mo 3*d* to build a coherent picture of its structural, magnetic, and electronic properties. We demonstrate cubic *Fm-3m* symmetry with rocksalt *B*-site order and no measurable Co or Mo antisite disorder within the sensitivity of powder diffraction, confirm a Co^{2+} $J_{\text{eff}} = 1/2$ Kramers doublet ground state from thermodynamics and XAS, and show that the observed antiferromagnetic order and spin-flop transition are consistent with dominant second-nearest-neighbor antiferromagnetic Co-O-Mo-O-Co superexchange interactions on the fcc lattice. Finally, we use surface photovoltage measurements to reveal a strong near-surface optical response with a prominent feature at 2.65 eV, placing BCMO in the broader landscape of Ba-based Mo and W double perovskites with visible-range optical transitions and suggesting potential spintronic and catalytic functionalities.

II. EXPERIMENTAL METHODS

A. Powder preparation

Polycrystalline BCMO was synthesized by two routes at the CoreLab Quantum Materials (HZB). First, a conventional solid-state reaction using stoichiometric $BaCO_3$, CoO, and MoO_3 was performed: the mixed powders were heated at 5 °C/min to 900 °C, calcined for 12 h, reground, and then heated at 5 °C/min to 1200 °C and sintered for 24 h, yielding BCMO with approximately 5% secondary phases [mainly $BaMoO_4$ and CoO, as identified by powder x-ray diffraction (PXRD)]. To improve phase purity, a sol-gel route was then adopted. Stoichiometric amounts (Ba:Co:Mo = 2:1:1) of $BaCO_3$ (99.99%), $Co(CH_3COO)_2$ (99.99%), and $(NH_4)_2MoO_4$ (prepared *in situ* by reacting MoO_3 with aqueous NH_3) were dissolved in deionized water with oxalic acid as a chelating agent. The solution was heated on a hot plate in air at 250 °C to remove water and form a metal-oxalate precursor, which was then calcined in air at 2 °C/min to 500 °C for 6 h and to 800 °C for 10 h with an intermediate grinding. The resulting powder was pressed into pellets and annealed at 3 °C/min to 1200 °C for 12 h in flowing argon, producing black BCMO powder with a reduced impurity fraction of 3.74% (quantified by Rietveld refinement of PXRD). Owing to the volatility of MoO_3, phase purity was found to be highly sensitive to precursor stoichiometry, annealing temperature, and heating rate; therefore, heating profiles were carefully controlled and crucibles sealed to minimize contamination and Mo loss. The sol-gel argon-annealed powder was used as a precursor for crystal growth. Parts of the polycrystalline boules from CZ crystal growth were selected and used for XAS, XPS, surface photovoltage (SPV) and thermodynamic measurements.

B. Crystal growth

Single-crystal growth was first initiated using an optical FZ furnace (Crystal Systems Corp., FZ-T-10000-H-VI-VPO) with four 300-W tungsten halide lamps. Initial growths in air at ambient pressure showed that BCMO melts incongruently, decomposing into multiple immiscible phases (e.g., Ba_2MoO_5, $CoMoO_4$, as identified by PXRD), and did not yield stable single crystals. Subsequent trials under 2 bars argon overpressure suppressed decomposition but still produced predominantly polycrystalline boules. Systematic improvements in the purity of the feed rods—via two or three cycles of annealing at 5 °C/min to 1200–1250 °C under argon for 24 h per cycle, each followed by slow cooling at 5 °C/min—

reduced impurity levels below approximately 3.74% and enhanced floating-zone stability, so that small single crystals (about $4 \times 3 \times 1$ mm^3) could be cut from the as-grown rods, as shown in Figs. 1(b) and 1(c). These results show that both argon overpressure and high-purity starting material are crucial to mitigate incongruent melting and preserve BCMO stoichiometry.

To further stabilize single-crystal growth, additional experiments were carried out using a CZ furnace (Mini Czochralski Oxypuller 05-03, Cyberstar) equipped with radio-frequency (rf) heating and an *in situ* weighing system on the pulling rod. Growth was attempted under flowing argon at 0.5 bar overpressure with nominal pulling rates of 0.5–1.0 mm/h and crystal and melt rotation rates of 10–20 rpm. Under these conditions, the charge exhibited partially molten regions and persistent solid chunks, preventing the establishment of a stable melt zone for seeded growth. Nevertheless, slow cooling from the melt reproducibly yielded small single crystals (about $3 \times 2.7 \times 0.2$ mm^3) with low impurity content. Laue backscattering patterns from these crystals exhibited sharp, well-defined spots consistent with the cubic symmetry of BCMO, confirming their single-crystal nature, as shown in Figs. 1(d) and 1(e).

C. Characterization

The structural parameters and phase purity of the polycrystalline and single-crystal BCMO samples were examined at room temperature by PXRD using a Bruker D8 diffractometer with Cu $K\alpha$ radiation. The PXRD data were analyzed by Rietveld refinement using the FullProf suite to extract lattice parameters, atomic positions, and phase fractions, by refining the main phase in the cubic *Fm-3m* space group (No. 225) [24]. Magnetic properties were measured using a superconducting quantum interference device (SQUID) magnetometer in the temperature range 2–300 K and in applied magnetic fields up to 70 kOe (1 kOe = 0.1 T). Heat capacity was measured in a physical property measurement system (PPMS, Quantum Design) between 2 and 300 K. Soft XAS at the Co $L_{2,3}$ edges was carried out at beamline TPS45 at the National Synchrotron Radiation Research Center (NSRRC), Hsinchu, Taiwan [25]. XPS analyses were performed using a monochromatic Al $K\alpha$ x-ray source (Focus 500, Specs), with a photon energy of 1400.00 eV, and an electron analyzer (Phoibos 100, Specs) at the Institute of Solar Fuels, HZB (see the Supplemental Material [26]).

The optical response was probed by SPV spectroscopy at room temperature using the fixed-capacitor method with a mechanical chopper at 8 Hz for both single crystals and powders, over a photon energy range 0.5–5 eV.

III. RESULTS

A. Structural characterization

PXRD analysis confirmed that BCMO crystallizes in an fcc structure with space group *Fm-3m* (No. 225) and regular undistorted rocksalt order consisting of regular BaO_{12} cuboctahedra and regular corner-sharing CoO_6 and MoO_6 octahedra. Ba^{2+} occupies the 8c Wyckoff position, while Co^{2+} occupies the 4b position, Mo^{6+} occupies the 4a position, and O^{2-} occupies the 24e position. All these atomic positions are fixed by the space group symmetry except for oxygen.

Antisite disorder is a key parameter in double perovskites because it suppresses the intensity of the superlattice reflections associated with *B*-site order [22]. In BCMO, we therefore allowed the Ba, Co, and Mo occupancies to vary during refinement; they do not deviate significantly from ideal stoichiometry. The PXRD pattern, including the superlattice reflections, and the Rietveld refinements are consistent with the ordered *Fm-3m* structure, with Co^{2+} and Mo^{6+} occupying the expected crystallographic sites and no measurable antisite disorder within the sensitivity of the measurement (1–2 %). The refined oxygen occupancy is consistent with a stoichiometric composition within the limits of PXRD. These results are also supported by the XPS spectrum for BCMO, which indicates the absence of Mo^{5+} in the polycrystalline sample. (Additional details on the analysis of magnetic susceptibility and XPS measurements are provided in the Supplemental Material [26].)

Figure 2 shows the refinement of the PXRD patterns of different samples of BCMO. The refinement factors are summarized for the sol-gel argon-annealed powder and both the CZ and FZ crystals of BCMO in Table I. Both polycrystalline samples, prepared by solid-state synthesis and the sol-gel method, were annealed in argon and contained a significant amount of impurities (approximately 3.74%). The structural refinement suggested that the main impurity phase is $BaMoO_4$ with space group $I41/a(88)$. Nevertheless, the argon-annealed powder has a slightly smaller amount of impurities than the reported powder (4.5%) [17], which was prepared in oxygen. Crystals grown by both the CZ and FZ methods have almost the same amount of impurities (2.33(2)%).

B. Magnetic properties

Figure 3 shows the temperature dependence of the magnetic susceptibility $\chi(T)$ and its inverse $1/\chi(T)$ for the polycrystalline sample and for single crystals oriented along [100] and [111], measured at 0.3, 1, and 10 kOe. The polycrystalline sample exhibits a pronounced concave curvature in $1/\chi(T)$, probably due to a higher $BaMoO_4$ impurity fraction than the single crystals, as confirmed by powder x-ray diffraction. Due to the difficulty in obtaining large, high-quality single crystals of BCMO, orientation-resolved measurements were performed on separate crystals grown by different methods: a [111]-oriented crystal from FZ growth in argon and a [100]-oriented crystal from CZ growth in argon. These different growth conditions lead to small but systematic differences in crystal quality and magnetic response, with the [100] crystal exhibiting an additional high-temperature feature around 300 K at high fields, consistent with residual impurities below the PXRD detection limit.

For the remainder of the quantitative magnetic analysis, we therefore focus on the [111] FZ crystal, which shows the cleanest intrinsic behavior as revealed by sharp Laue patterns, the absence of a large diamagnetic offset, and the lowest impurity content. All samples, regardless of morphology or growth method, exhibit the same Néel temperature of $T_N = 20.1(1)$ K. The inverse susceptibility of all samples deviates strongly from linear Curie-Weiss behavior between

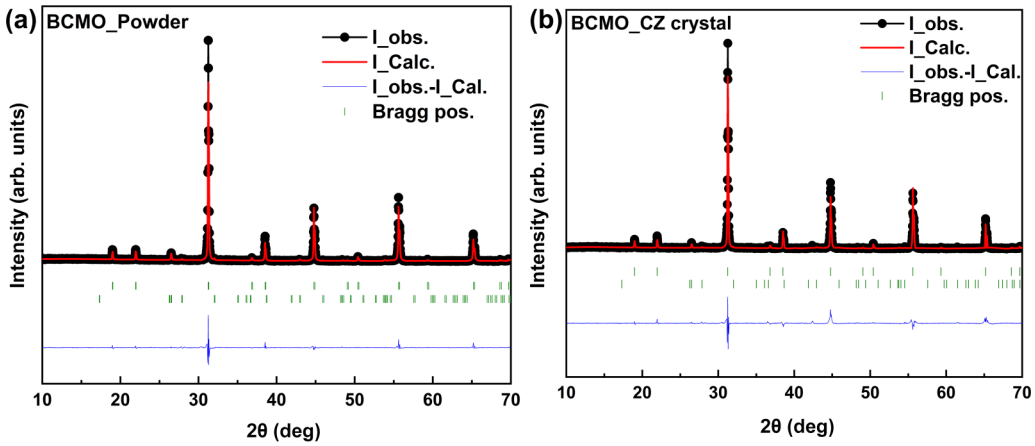


FIG. 2. Rietveld refinement of the x-ray powder diffraction of BCMO: (a) sol-gel annealed powder with 3.74% $BaMoO_4$, (b) CZ crystal with 2.31% $BaMoO_4$. The data are represented by the black circles, while the refinement is given by the red line which includes both the BCMO (top row of green marks) and $BaMoO_4$(bottom row of green marks) phases. The blue line gives the difference between fit and data.

about 30 and 150 K, closely resembling the response reported for BCWO and demonstrating that a simple Curie-Weiss law is not adequate [11,27,28]. This nonlinearity is naturally understood in terms of thermal population of low-lying excited states within the Co^{2+} $^4T_1$ multiplet in an octahedral crystal field with substantial spin-orbit coupling, rather than being attributable solely to magnetic interactions or extrinsic defects [28]. For high-spin octahedral Co^{2+} ($3d^7$), the $^4T_{1g}$ ground term carries an effective orbital angular momentum $l = 1$; spin-orbit coupling λ splits this triplet into low-lying $J_{\text{eff}} = 1/2$, 3/2, and 5/2 multiplets separated by energies of order $|\lambda|$. This level scheme and the associated low-lying excited states are well established for octahedral Co^{2+} complexes [11,16].

To describe the Co^{2+} magnetic response quantitatively, the susceptibility of BCMO is simulated for the fields applied using a cluster model with parameters derived from the XAS analysis discussed later. The antiferromagnetic interactions between the Co ions are considered, using Weiss's molecular field approach $\chi = M/(H + wM)$. The fitted molecular-field parameter w accounts for the antiferromagnetic Co-Co interactions and produces a positive offset in the inverse susceptibility. For both applied fields we obtain a very good match between experiment and calculation for $T > 100$ K (see Fig. 4), with $w = 20$ mol/cm^3 at 0.3 kOe and $w = 21$ mol/cm^3 at 10 kOe. In the simple mean-field limit, w can be expressed as an effective Weiss temperature through $\theta_W = -Cw$, giving $\theta_W \approx -37$ K, which indicates a weak frustration in BCMO.

Isothermal magnetization measurements provide evidence for the slight anisotropy of BCMO, as seen from nonlinear $M(H)$ responses and their field derivatives for crystals oriented along [100] and [111]. Figure 5 represents the magnetization curves and the first derivative of magnetization for the two crystalline samples at $T = 3$ K. The measurement revealed that the magnetization of BCMO has nonlinear behavior for the [100] and [111] crystals. The first derivative of magnetization of [100] and [111] shows a pronounced peak at 26.5 kOe consistent with a spin-flop transition. In a classical easy-axis two-sublattice antiferromagnet, a spin-flop transition occurs when the magnetic field ($H_{\text{sf}} = 26.5$ kOe) is applied along the easy axis; below H_{sf}, the sublattice moments are antiparallel and collinear with the field, whereas above H_{sf} the staggered magnetization reorients to lie nearly perpendicular to the field, with a small canting toward H.

Neutron powder diffraction on BCMO has established a type-II antiferromagnetic structure with propagation vector $\mathbf{k} = (1/2, 1/2, 1/2)$, corresponding to ferromagnetic Co layers perpendicular to [111] stacked antiferromagnetically along this direction [17]. This suggests dominant antiferromagnetic second-nearest-neighbor exchange interactions via 180° Co-O-Mo-O-Co pathways, while the frustrated first-nearest-neighbor interaction is much weaker. Although the spin direction was not determined, this structure admits several symmetry-related domains with different equivalent orientations of the local easy axis relative to the crystallographic

TABLE I. Rietveld refinement parameters for BCMO samples, including the lattice parameter (a), the R factors including the profile Rfactor (R_p), weighted-profile R factor (R_{wp}), and the expected R factor (R_{exp}), the atomic positions of oxygen in the x direction [x(O)], and the occupancy of oxygen (O_{occ}).

	Impurities (%) $BaMoO_4$	a (Å)	R_p (%)	R_{wp} (%)	R_{exp} (%)	χ^2	x(O)	O_{occ}
Sol-gel Annealed	3.74(3)	8.088	3.99	5.93	2.65	5.01	0.26	1
Crystal CZ	2.31(2)	8.088	5.16	7.81	2.81	7.70	0.25	1
Crystal FZ	2.35(2)	8.088	4.25	8.60	3.75	8.00	0.25	1
Reported [17]	4.5	8.086	4.26	5.76	3.69	2.43	0.25	1

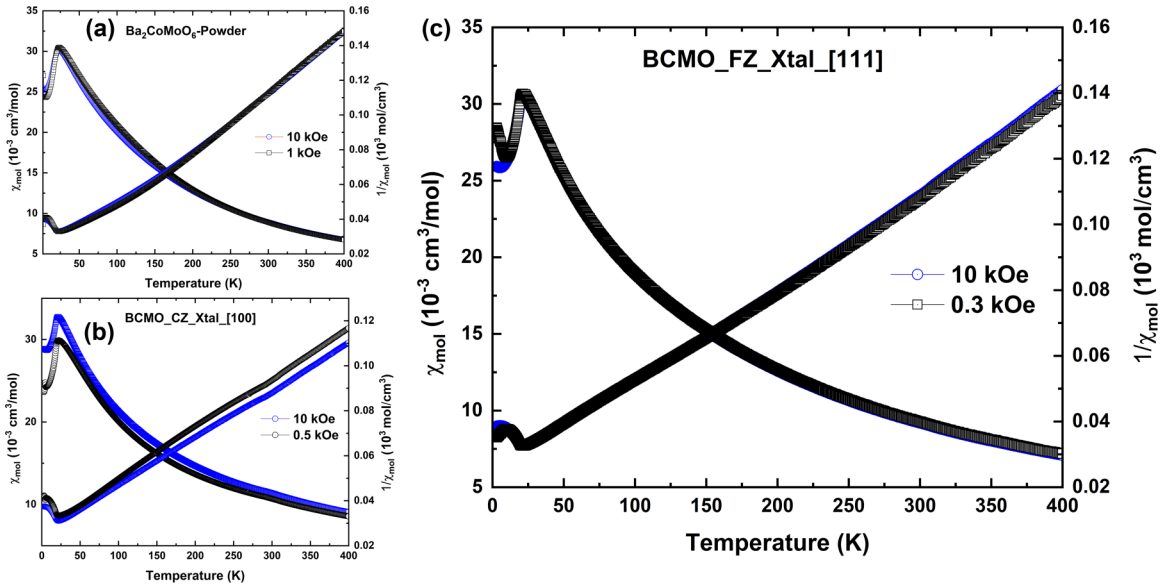


FIG. 3. Temperature dependence of magnetic susceptibility (left-hand y axis) and inverse susceptibility (right-hand y axis) of BCMO samples at 0.3 and 10 kOe: (a) polycrystalline powder, (b) CZ crystal with field applied along the [100] direction, and (c) FZ crystal with field along the [111] direction.

axes. In our single crystal, both $H \parallel [100]$ and $H \parallel [111]$ have substantial projections onto the local easy axes of at least some domains, so a spin-flop or spin-reorientation transition appears in the magnetization for both field directions.

Very similar behavior is observed in isostructural Ba_2CoWO_6, where spin-flop transitions occur for $H \parallel [100]$ and $H \parallel [111]$, but not for $H \parallel [110]$, suggesting a common easy-axis orientation in the $Ba_2CoB'O_6$ ($B' =$ Mo, W) family [18]. The observation of a spin-flop transition implies a finite magnetic anisotropy, which stabilizes an antiferromagnetic ground state with a preferred spin orientation [29]. The spin-flop field reflects the balance between anisotropy energy and exchange interactions. Taken together, these results indicate that Ba_2CoMoO_6 is governed by antiferromagnetic exchange interactions and weak anisotropy.

C. Heat capacity

Figure 6(a) shows the heat capacity of BCMO single crystals up to 50 K and of the polycrystalline boules up to 200 K, revealing a second-order anomaly at $T_N = 20$ K consistent with the onset of long-range antiferromagnetic order inferred from susceptibility data. No significant change was noticed in the heat capacity under different applied magnetic fields up to 90 kOe and the Néel temperature is almost field independent for all samples. The transition peak is noticeably sharper in the crystals than in powder, reflecting higher sample quality and reduced disorder broadening in the single crystals. To isolate the magnetic contribution, the lattice heat capacity of the polycrystalline sample was modeled between 50 and 170 K, well above the magnetic ordering temperature T_N, using a Debye-Einstein scheme with one Debye and one Einstein

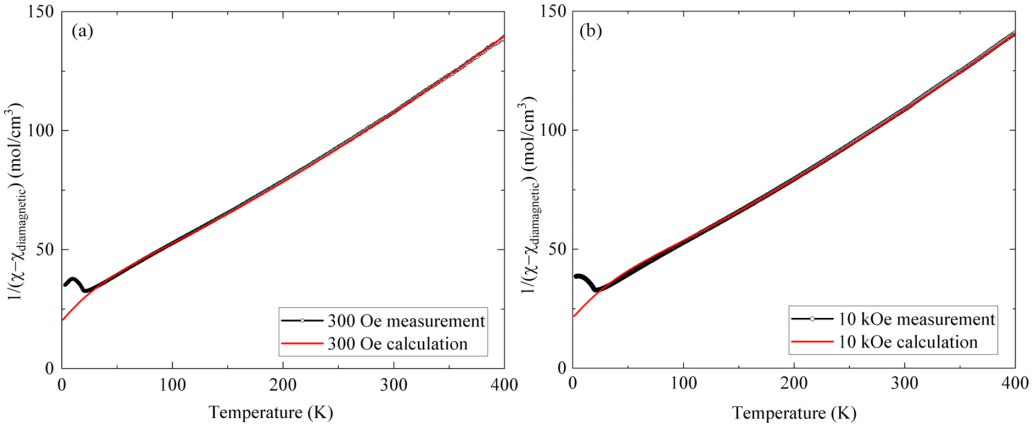


FIG. 4. Temperature dependence of inverse magnetic susceptibility of BCMO samples at (a) 0.3 kOe and (b) 10 kOe compared with simulation based on cluster model derived with parameters derived from XAS measurements.

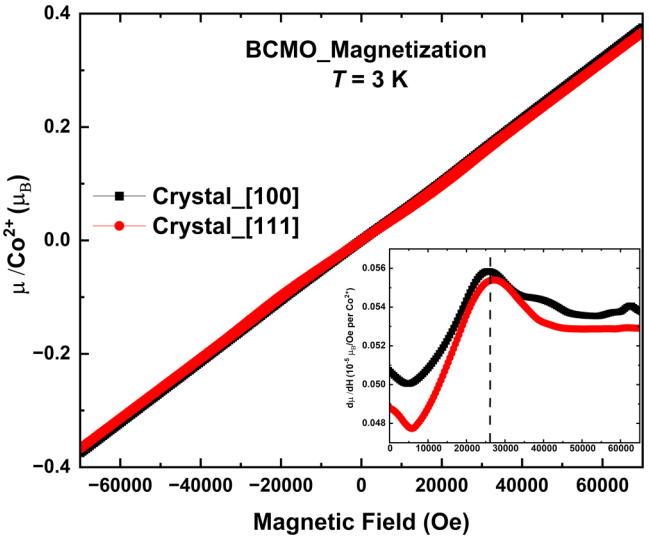


FIG. 5. Isothermal magnetization of different BCMO crystals with field applied along the [100] and [111] directions at $T = 3$ K. The inset shows the derivative of the effective moment per Co^{2+} ion for the directions [100] (black) and [111] (red). The dashed line represents a spin-flop transition around 26.5 kOe for both the [100] and [111] directions.

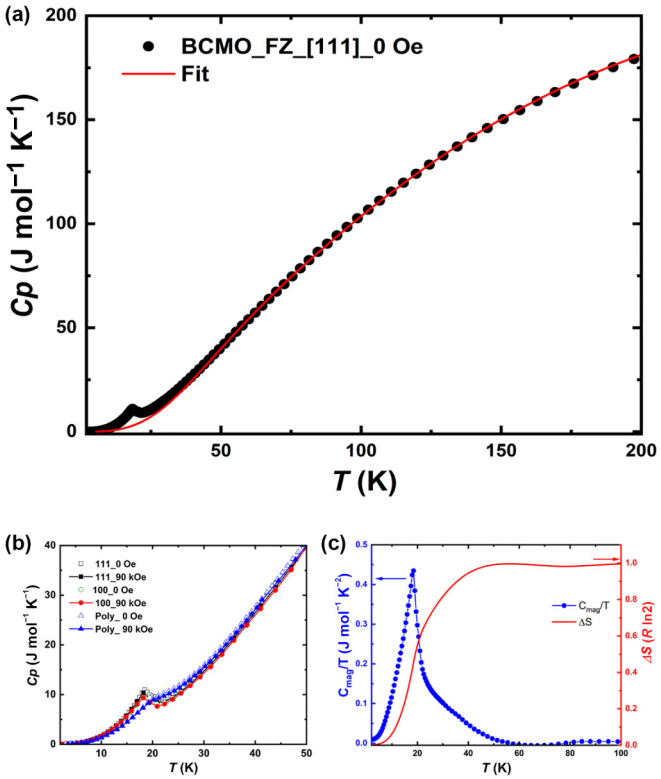


FIG. 6. (a) The heat capacity of the BCMO polycrystalline sample at zero field fitted by Debye and Einstein models to subtract the magnetic contribution of the heat capacity in the temperature range 50–150 K. (b) Heat capacity of BCMO crystals for magnetic field applied along the [100] and [111] directions and for the sol-gel polycrystals. (c) Magnetic contribution of the heat capacity over temperature (left-hand axis) for the polycrystalline sample in zero field. The entropy change is shown on the right-hand axis in units of $R \ln 2$.

branch in a 51.5:48.5 weight ratio, according to the equation

$$c_p(T) = 3Rn\left(0.515\left(\frac{T}{\theta_D}\right)^3 3\int_0^{\frac{\theta_D}{T}} \frac{x^4\, e^x}{(e^x-1)^2}\, dx + 0.485\left(\frac{\theta_E}{T}\right)^2 \frac{e^{\theta_E/T}}{(e^{\theta_E/T}-1)^2}\right),$$

where R is the universal gas constant, n is the number of ions per formula unit, which is $n = 10$ for BCMO, and θ_D and θ_E are the Debye and Einstein temperatures, respectively. The resulting fit yields $\theta_D = 277(4)$ K and $\theta_E = 568(5)$ K, which provide a reasonable description of the phonon background over the chosen window and a stable baseline for extracting the magnetic heat capacity, c_{mag}, by extrapolating to low temperature and subtracting from the measured data. The extracted magnetic heat capacity and entropy changes are shown in Fig. 6(c). The weak drop in c_{mag}/T between 60 and 80 K is most likely due to the combined effects of phonon-subtraction uncertainty and residual impurities in the sample.

The entropy change ΔS was calculated by integrating c_{mag}/T in the range 2–100 K. The magnetic entropy saturates at about 50 K at the value 5.5(1) J mol^{-1} K^{-1} or $0.95(2)R \ln 2$. The saturation value is consistent within uncertainty with a doublet ground state described by $J_{eff} = 1/2$, for which $\Delta S = R \ln(2J+1) = R \ln 2$. This is similar to Ba_2CoWO_6, which also has $J_{eff} = 1/2$ [18]. Above the Néel temperature, up to 50 K, 41% of the entropy is released. The extended release of entropy above T_N suggests the persistence of correlated magnetic fluctuations well above T_N. The slightly reduced value of entropy change of $0.95(2)R \ln 2$ by $T = 50$ K could be attributed to a conservative phonon-background subtraction together with the minor secondary phases, resulting in slight underestimation of the extracted entropy.

IV. ELECTRONIC STRUCTURE

A. X-ray absorption spectroscopy

To probe the electronic and magnetic properties of BCMO we performed temperature-dependent XAS using the inverse partial fluorescence yield method [30,31], which is suitable for extremely insulating samples, in a similar manner to what is reported in Ref. [32]. XAS is extremely sensitive to the local electronic structure, and when combined with theoretical modeling to simulate the measured spectra, it is possible to obtain information about the ground-state quantum numbers and effective crystal-field parameters [10–13,33,34]. Part of the residual polycrystalline boules from CZ crystal growth was mounted in an aluminum sample holder and cleaved in ultrahigh-vacuum conditions before being transferred *in vacuo* to the measurement chamber with a base pressure of about 10^{-11} mbar.

Figure 7 shows the temperature-dependent isotropic Co $L_{2,3}$ XAS spectra of BCMO. In XAS the measured spectra are separated into the two L_2 and L_3 edges due to $2p$ spin-orbit coupling. The obtained line shape is characteristic of a Co^{2+} valence, which we will explain with our calculations. The temperature dependence originates from the thermal population of low-lying excited states with increasing temperature.

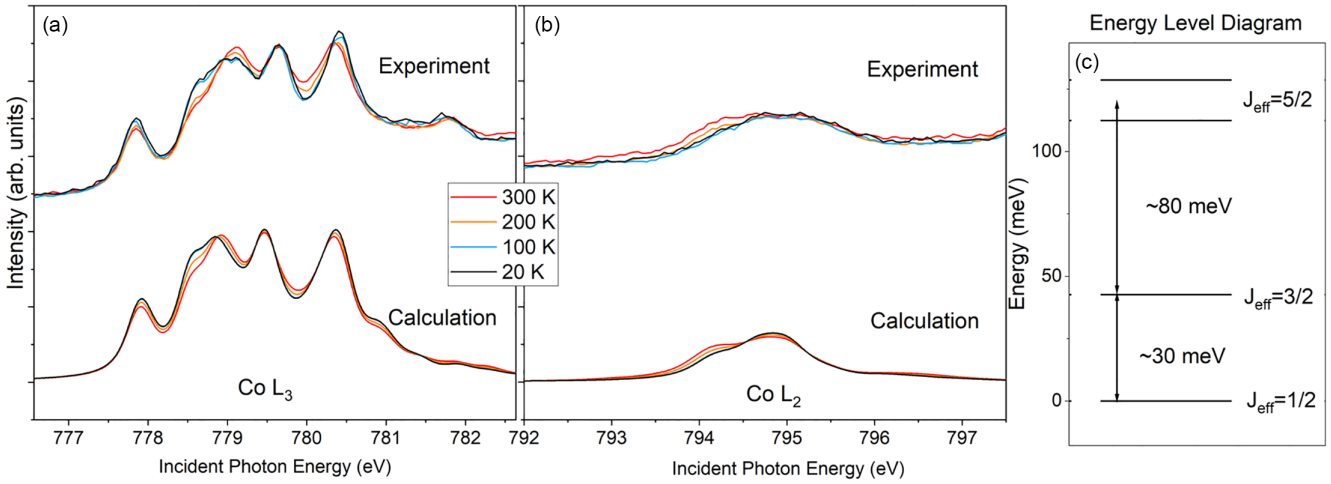


FIG. 7. Experimental and calculated temperature dependence of the XAS spectra of Ba_2CoMoO_6 for the (a) L_3 and (b) L_2 Co edges and (c) the corresponding energy-level diagram for the calculation without core hole.

This behavior is expected for high-spin Co^{2+} ions in octahedral coordination [11].

To obtain further information about the electronic structure of the compound, we performed full-multiplet configuration-interaction cluster calculations for a CoO_6 cluster using the O_h point group. Hybridization parameters were obtained from Wannierized density functional theory (DFT) band structure calculations [35] using the FPLO code [36]. The cluster-interaction calculations were performed with the QUANTY code [35,37–39]. The full set of parameters used in our calculations is listed as Ref. [40]. Our calculations include $3d$-$3d$ and $2p$-$3d$ Coulomb interactions, spin-orbit coupling for both the $2p$ and $3d$ shells, hybridization with oxygen ligands, and crystal-field effects. We obtain a very good agreement between experiment and calculation, implying that our model accurately captures most details of the local electronic structure of Co^{2+} ions in this material. Importantly, the XAS results confirm that Co ions in this material are divalent, Co^{2+}. Charge neutrality then requires Mo to be in the hexavalent Mo^{6+} oxidation state, consistent with the observed insulating character of the compound. Furthermore, we performed XPS analyses to detect any absorption from both Mo^{5+} and Mo^{6+} in the polycrystalline sample. The Mo $3d$ XPS spectrum shows a main doublet in the Mo^{6+} binding-energy region. No clear separate feature attributable to Mo^{5+} is observed in the raw spectrum, suggesting that Mo is predominantly in the hexavalent state. (Additional details on the analysis of XPS measurements are provided in the Supplemental Material [26].)

The parameters that we have obtained from the XAS analysis (listed as Ref. [40]) serve as a good starting point for describing the near-ground-state properties of the material. Now we need to consider that the presence of the core hole in the XAS process may affect the radial extent of the $3d$ orbital. This implies that the parameters in describing the electronic states in core-hole-free experiments may be somewhat different [41–43]. For example, the crystal field felt by the $3d$ electrons as well as the hybridization strength between the $3d$ and the ligands tend to be smaller in the presence of the core hole. To reproduce the magnetic susceptibility data, we have to increase the 10 Dq value to 0.85 eV and the hybridization strength by 20%, and reduce the spin-orbit-coupling parameter to 46 meV. With these adjustments we were able to obtain an excellent match with the experiment (see Fig. 4). We then estimate the g factor using the relation $\Delta E = g\mu_B B$, where ΔE is the splitting of the doublet due to magnetic field. In a calculation with applied field of 6 T at 0 K, we obtain a value of $g = 4.36$.

From our model we find the first low-lying spin-orbit coupling excited state at 30 meV, as shown in Fig. 7(c).

B. Surface photovoltage spectroscopy

SPV spectroscopy is a contactless, surface-sensitive probe of illumination-induced changes in near-surface band bending and photocarrier separation, and thus reports on optically driven excitations in the vicinity of the surface [44,45]. In Ba_2CoMoO_6 (BCMO), the SPV spectrum (Fig. 8) exhibits a clear onset near 1.5 eV, a pronounced maximum at 2.65 eV, and a broad decay in intensity up to about 4.5 eV, showing that the near-surface photoresponse is dominated by a distinct transition manifold rather than a featureless background. Because SPV is inherently sensitive to surface and space-charge-region physics, the low-energy onset should be interpreted as an effective photoresponse threshold influenced by band bending and defect states, not as a direct measurement of the bulk band gap [44–46].

The strong SPV maximum at 2.65 eV is naturally associated with the dominant crystal-field or charge-transfer transition of the Co-O-Mo network on the face-centered-cubic lattice. Its energy scale is consistent with reported optical gaps in related Ba-based double perovskites: Ba_2CoWO_6 shows a cubic *Fm-3m* structure with an optical gap of about 2.4–2.6 eV from UV-visible and SPV analysis [18], while Ba_2CaMoO_6 and other Ba_2AMoO_6 compounds exhibit direct gaps in the range 2.3–2.8 eV from combined DFT and diffuse-reflectance measurements [47–49]. In this context, the 2.65-eV feature in BCMO fits naturally into the Mo and W double-perovskite landscape and indicates that the Co-O-Mo manifold hosts a robust, visible-range optical transition that efficiently drives surface photovoltage [50].

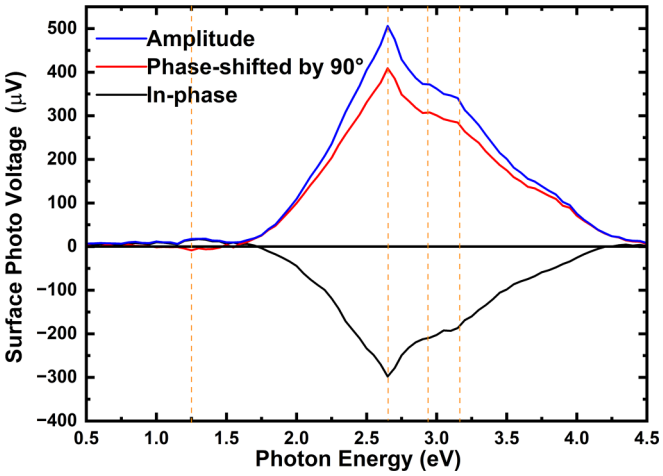


FIG. 8. Surface photovoltage (SPV) measurement of polycrystalline pellets of BCMO plotted as a function of photon energy: the in-phase signal (x component) (black), the signal that is phase shifted by 90° (y component) (red), and the SPV amplitude (composed of both x and y components) (blue). The dashed orange lines represent the absorption of the BCMO phase.

The SPV spectrum reflects multiple photoactive channels, arising from a combination of intrinsic electronic transitions and surface- or defect-related processes [44,45]. A more detailed separation of *d-d*, charge-transfer, and band-to-band contributions will require combining SPV with bulk-sensitive optical probes, such as ellipsometry or diffuse reflectance spectroscopy, and targeted first-principles calculations [49,50]. Within the present data, however, the robust SPV response and prominent 2.65-eV feature already demonstrate that BCMO hosts a strong, near-surface optoelectronic response in the visible to near-UV range, comparable in energy scale to Ba_2CoWO_6 and Ba_2CaMoO_6 but realized here in a spin-orbit-entangled fcc antiferromagnet. This combination of antiferromagnetic order, Co-based crystal-field physics, and efficient photovoltage generation highlights Ba_2CoMoO_6 as a promising platform for spintronic optoelectronic devices and photocatalytic or photoelectrochemical applications, where simultaneous control of magnetic order and interfacial charge separation is desired [50–52].

V. CONCLUSIONS

This work establishes high-quality Ba_2CoMoO_6 (BCMO) single crystals as a robust platform for studying intrinsic magnetic and electronic properties of face-centered-cubic (fcc) antiferromagnets with strong spin-orbit coupling. Optimized floating-zone and top-seeded solution growth under argon atmosphere produced crystals with reduced $BaMoO_4$ impurity fractions compared to the powder samples, confirming the cubic *Fm-3m* structure with lattice parameter $a = 8.088$ Å. Rietveld refinements of powder xray diffraction data, including the superlattice reflections associated with B site order, show that Ba, Co, and Mo occupancies remain close to ideal stoichiometry and that oxygen occupancy is stoichiometric within experimental uncertainty, indicating rocksalt ordering of Co and Mo and no measurable antisite disorder or mixed valences as supported by XPS.

Magnetic susceptibility and heat capacity measurements consistently reveal long-range antiferromagnetic ordering at $T_N = 20.1(1)$ K, which is unaffected by applied fields up to 90 kOe. Quantitative analysis of the [111] single-crystal susceptibility using the cluster model derived from XAS analysis reproduces the measured curve. The fitted molecular-field parameters give an effective Weiss temperature of -37 K. Isothermal magnetization reveals a spin-flop transition at 26.5 kOe for both the [100] and [111] orientations, indicating weak magnetocrystalline anisotropy and ordered-moment components along these crystallographic directions.

The Debye-Einstein fitting of the heat capacity provides the phonon background needed to isolate the magnetic contribution c_{mag}, from which the magnetic entropy is obtained by integrating c_{mag}/T. The fact that the entropy saturates close to $R \ln 2$ indicates that, over the measured temperature range, the thermally accessible magnetic degrees of freedom correspond to a two-level manifold. For Co^{2+} in the present octahedral environment, this is consistent with a Kramers-doublet ground state produced by the combined action of spin-orbit coupling and crystal-field splitting, in agreement with the $J_{eff} = 1/2$ state inferred from XAS. X-ray absorption spectroscopy independently verifies the Co^{2+} valence state, the local octahedral crystal-field scheme, and the doubly degenerate ground state with $J_{eff} = 1/2$ character and yields a g factor $g = 4.36$, consistent with the enhanced moment observed in susceptibility. For Mo, XPS Mo-edge spectroscopy indicates Mo^{6+} as supported by charge balance, the Co^{2+} assignment, and the absence of reduced Mo phases in the diffraction data. Surface photovoltage spectroscopy suggests a strong optical response linked to crystal-field and band-structure transitions, implying potential for optoelectronic applications, though bulk optical measurements (ellipsometry, diffuse reflectance) would complement these surface-sensitive SPV data.

To summarize, these results position Ba_2CoMoO_6 alongside Ba_2CoWO_6 as a model weakly frustrated fcc antiferromagnet, distinguished by its robust $J_{eff} = 1/2$ ground state, modest anisotropy, and accessible spin-flop behavior. The weak-frustration assignment is suggested by the release of 41% of the expected entropy above the Néel temperature, the effective Weiss temperature of -37 K, as well as the microscopic description of the magnetic response provided by the XAS-derived cluster mode. Future work will combine single-crystal neutron diffraction, bulk optical spectroscopy, and first-principles calculations. This approach will refine the magnetic structure and clarify electronic-level assignments. Additionally, assess spintronic and energy-conversion applications which are suggested by the spin-flop transition and strong photovoltage response. The transition enables field-controlled reorientation of the Néel vector. Consequently, this mechanism may strongly modulate transport signals.

ACKNOWLEDGMENTS

We acknowledge the CoreLab Quantum Materials at Helmholtz Zentrum Berlin für Materialien und Energie (HZB), Germany, where the powder and single-crystal

samples of Ba_2CoMoO_6 were synthesized and characterized. The authors acknowledge the support of Igal Levine and Thomas Dittrich from the Solar Energy Division, HZB, for performing the surface photovoltage measurements. We acknowledge Christian Höhn from the Institute of Solar Fuels, HZB, for performing the x-ray photoemission spectroscopy. M.M.F.-C. greatly acknowledges funding from the Deutsche Forschungsgemeinschaft (DFG, German Research Foundation), Grant No. 387555779. Work at MPI-CPfS Dresden and HZB was partially supported by the Deutsche Forschungsgemeinschaft (DFG, German Research Foundation) through SFB 1143 (Project No. 247310070). The authors acknowledge the support from the Max Planck-POSTECH-Hsinchu Center for Complex Phase Materials.

The authors declare no conflict of interest.

DATA AVAILABILITY

There are no publicly available research data or software supporting this manuscript. Requests for further information or data should be sent to the authors.

[1] K. I. Kobayashi, T. Kimura, H. Sawada, K. Terakura, and Y. Tokura, Room-temperature magnetoresistance in an oxide material with an ordered double-perovskite structure, Nature (London) **395**, 677 (1998).

[2] H. Mutch, O. Mustonen, H. C. Walker, P. J. Baker, G. B. G. Stenning, F. C. Coomer, and E. J. Cussen, Long- and short-range magnetism in the frustrated double perovskite Ba_2MnWo_6, Phys. Rev. Mater. **4**, 014408 (2020).

[3] S. Liu, Y. Cheng, S. Yan, J. He, L. Deng, and H. Luo, Unravelling the electromagnetic behavior in ordered double-perovskite Sr_2FeMoO_6, J. Electron. Mater. **51**, 3430 (2022).

[4] L. A. Muscarella and E. M. Hutter, Halide double-perovskite semiconductors beyond photovoltaics, ACS Energy Lett. **7**, 2128 (2022).

[5] D. C. Binwal, P. P. Mudoi, D. P. Panda, and P. Vishnoi, Molybdenum chloride double perovskites: Dimensionality control of optical and magnetic properties, Chem. Sci. **14**, 3982 (2023).

[6] H. L. Feng, S. Calder, M. P. Ghimire, Y. H. Yuan, Y. Shirako, Y. Tsujimoto, Y. Matsushita, Z. Hu, C. Y. Kuo, L. H. Tjeng, T. W. Pi, Y. L. Soo, J. He, M. Tanaka, Y. Katsuya, M. Richter, and K. Yamaura, Ba_2NiOsO_6: A Dirac-Mott insulator with ferromagnetism near 100 K, Phys. Rev. B **94**, 235158 (2016).

[7] M. Vogl, R. Morrow, A. A. Aczel, R. B. Rodriguez, A. U. B. Wolter, S. Wurmehl, S. Aswartham, and B. Büchner, Complex magnetic properties in the mixed $4f-5d$ double perovskite iridates X_2ZnIrO_6 (X = Nd, Sm, Eu, Gd), Phys. Rev. Mater. **4**, 054413 (2020).

[8] A. Rachedi, R. Baghdad, and A. Nacef, Magnetic, optoelectronic and thermodynamic properties of the double perovskite Ba_2NiWO_6 in its stable antiferromagnetic phase, Optik **227**, 166032 (2021).

[9] H. L. Feng, Z. Deng, C. U. Segre, M. Croft, S. H. Lapidus, C. E. Frank, Y. Shi, C. Jin, D. Walker, and M. Greenblatt, High-pressure synthesis of double perovskite Ba_2NiIrO_6: In search of a ferromagnetic insulator, Inorg. Chem. **60**, 1241 (2021).

[10] T. Burnus, Z. Hu, M. W. Haverkort, J. C. Cezar, D. Flahaut, V. Hardy, A. Maignan, N. B. Brookes, A. Tanaka, H. H. Hsieh, H. J. Lin, C. T. Chen, and L. H. Tjeng, Valence, spin, and orbital state of Co ions in one-dimensional $Ca_3Co_2O_6$: An x-ray absorption and magnetic circular dichroism study, Phys. Rev. B **74**, 245111 (2006).

[11] T. Burnus, Z. Hu, H. H. Hsieh, V. L. J. Joly, P. A. Joy, M. W. Haverkort, H. Wu, A. Tanaka, H. J. Lin, C. T. Chen, and L. H. Tjeng, Local electronic structure and magnetic properties of $LaMn_{0.5}Co_{0.5}O_3$ studied by x-ray absorption and magnetic circular dichroism spectroscopy, Phys. Rev. B **77**, 125124 (2008).

[12] H. J. Lin, Y. Y. Chin, Z. Hu, G. J. Shu, F. C. Chou, H. Ohta, K. Yoshimura, S. Hébert, A. Maignan, A. Tanaka, L. H. Tjeng, and C. T. Chen, Local orbital occupation and energy levels of Co in Na_xCoO_2: A soft x-ray absorption study, Phys. Rev. B **81**, 115138 (2010).

[13] Y. Y. Chin, Z. Hu, H. J. Lin, S. Agrestini, J. Weinen, C. Martin, S. Hébert, A. Maignan, A. Tanaka, J. C. Cezar, N. B. Brookes, Y. F. Liao, K. D. Tsuei, C. T. Chen, D. I. Khomskii, and L. H. Tjeng, Spin-orbit coupling and crystal-field distortions for a low-spin $3d^5$ state in $BaCoO_3$, Phys. Rev. B **100**, 205139 (2019).

[14] Y. Y. Chin, Z. Hu, Y. Shimakawa, J. Yang, Y. Long, A. Tanaka, L. H. Tjeng, H. J. Lin, and C. T. Chen, Charge and spin degrees of freedom in A-site ordered $YCu_3Co_4O_{12}$ and $CaCu_3Co_4O_{12}$, Phys. Rev. B **103**, 115149 (2021).

[15] Q. Che, M. Ghiasi, L. Braglia, M. L. J. Peerlings, S. Mauri, P. Torelli, P. de Jongh, and F. M. F. de Groot, Operando soft x-ray absorption of $LaMn_{1-x}Co_xO_3$ perovskites for CO oxidation, ACS Catal. **14**, 11243 (2024).

[16] F. Lloret, M. Julve, J. Cano, R. Ruiz-García, and E. Pardo, Magnetic properties of six-coordinated high-spin cobalt(II) complexes: Theoretical background and its application, Inorganica Chim. Acta **361**, 3432 (2008).

[17] M. J. Martínez-Lope, J. A. Alonso, M. T. Casais, and M. T. Fernández-Díaz, Preparation, crystal and magnetic structure of the double perovskites Ba_2CoBO_6 (B = Mo, W), Eur. J. Inorg. Chem. **2002**, 2463 (2002).

[18] A. R. N. Hanna, A. T. M. N. Islam, C. Ritter, S. Luther, R. Feyerherm, and B. Lake, Growth of Ba_2CoWO_6 single crystals and their magnetic, thermodynamic and electronic properties, J. Phys. Condens. Matter **36**, 505801 (2024).

[19] Q. Yao, S. Y. Lv, Z. Yu, Y. C. Chang, C. W. Pao, Z. Hu, L. M. Yang, X. Huang, Q. Shao, and J. Lu, Face-centered cubic ruthenium nanocrystals with promising thermal stability and electrocatalytic performance, ACS Catal. **13**, 11023 (2023).

[20] R. L. Zhang, L. Damewood, Y. J. Zeng, H. Z. Xing, C. Y. Fong, L. H. Yang, R. W. Peng, and C. Felser, Two prospective Li-based half-Heusler alloys for spintronic applications based on structural stability and spin–orbit effect, J. Appl. Phys. **122**, 013901 (2017).

[21] T. Hirama, N. Tsujii, H. Kitazawa, and G. Kido, La-substitution effects on double perovskite compound Ba_2CoMoO_6, Phys. B Condens. Matter **359–361**, 1336 (2005).

[22] C. Meneghini, S. Ray, F. Liscio, F. Bardelli, S. Mobilio, and D. D. Sarma, Nature of "disorder" in the ordered double perovskite Sr_2FeMoO_6, Phys. Rev. Lett. **103**, 046403 (2009).

[23] X. Wang, J. Zhang, Z. Pan, D. Lu, M. Pi, X. Ye, C. Dong, J. Chen, K. Chen, F. Radu, S. Francoual, S. Agrestini, Z. Hu, C. F. Chang, A. Tanaka, K. Yamaura, Y. Shen, and Y. Long, X-ray absorption spectroscopic study of the transition-metal-only double perovskite oxide Mn_2CoReO_6, J. Phys. Chem. C **128**, 15668 (2024).

[24] J. Rodríguez-Carvajal, Recent advances in magnetic structure determination by neutron powder diffraction, Phys. B Condens. Matter **192**, 55 (1993).

[25] H. M. Tsai, H. W. Fu, C. Y. Kuo, L. J. Huang, C. S. Lee, C. Y. Hua, K. Y. Kao, H. J. Lin, H. S. Fung, S. C. Chung, C. F. Chang, A. Chainani, L. H. Tjeng, and C. T. Chen, A submicron soft x-ray active grating monochromator beamline for ultra-high resolution angle-resolved photoemission spectroscopy, AIP Conf. Proc. **2054**, 060047 (2019).

[26] See Supplemental Material at http://link.aps.org/supplemental/10.1103/6l9n-djww for additional details on analysis of magnetic susceptibility and XPS measurements. Supporting Information available for this article includes additional magnetic characterization of Ba_2CoMoO_6, comprising a Lloret-model treatment of the [111] crystal to account for the spin-orbit-coupled Co^{2+} response. It also includes XPS measurements and core-level fitting of the Mo 3*d* region, which establish the exclusively Mo^{6+} valence state. The relevant data are presented in Figs. SI-1 through SI-3 and Tables SI-1–SI-2, which includes Refs. [16,53–57].

[27] S. Mugiraneza and A. M. Hallas, Tutorial: A beginner's guide to interpreting magnetic susceptibility data with the Curie-Weiss law, Commun. Phys. **5**, 95 (2022).

[28] P. M. Sarte, R. A. Cowley, E. E. Rodriguez, E. Pachoud, D. Le, V. García-Sakai, J. W. Taylor, C. D. Frost, D. Prabhakaran, C. MacEwen, A. Kitada, A. J. Browne, M. Songvilay, Z. Yamani, W. J. L. Buyers, J. P. Attfield, and C. Stock, Disentangling orbital and spin exchange interactions for Co^{2+} on a rocksalt lattice, Phys. Rev. B **98**, 024415 (2018).

[29] A. N. Bogdanov, A. V. Zhuravlev, and U. K. Rößler, Spin-flop transition in uniaxial antiferromagnets: Magnetic phases, reorientation effects, and multidomain states, Phys. Rev. B **75**, 094425 (2007).

[30] A. J. Achkar, T. Z. Regier, E. J. Monkman, K. M. Shen, and D. G. Hawthorn, Determination of total x-ray absorption coefficient using non-resonant x-ray emission, Sci. Rep. **1**, 182 (2011).

[31] A. J. Achkar, T. Z. Regier, H. Wadati, Y. J. Kim, H. Zhang, and D. G. Hawthorn, Bulk sensitive x-ray absorption spectroscopy free of self-absorption effects, Phys. Rev. B **83**, 081106(R) (2011).

[32] M. M. Ferreira-Carvalho, S. Rößler, C. F. Chang, Z. Hu, S. M. Valvidares, P. Gargiani, M. W. Haverkort, P. K. Mukharjee, P. Gegenwart, A. A. Tsirlin, and L. H. Tjeng, Trigonal distortion in the Kitaev candidate honeycomb magnet $BaCo_2(AsO_4)_2$, Phys. Rev. B **112**, 125135 (2025).

[33] F. M. F. de Groot, X-ray absorption and dichroism of transition metals and their compounds, J. Electron Spectrosc. Relat. Phenom. **67**, 529 (1994).

[34] A. Tanaka and T. Jo, Resonant 3*d*, 3*p* and 3*s* photoemission in transition metal oxides predicted at 2*p* threshold, J. Phys. Soc. Jpn. **63**, 2788 (1994).

[35] M. W. Haverkort, M. Zwierzycki, and O. K. Andersen, Multiplet ligand-field theory using Wannier orbitals, Phys. Rev. B **85**, 165113 (2012).

[36] K. Koepernik and H. Eschrig, Full-potential nonorthogonal local-orbital minimum-basis band-structure scheme, Phys. Rev. B **59**, 1743 (1999).

[37] M. W. Haverkort, G. Sangiovanni, P. Hansmann, A. Toschi, Y. Lu, and S. Macke, Bands, resonances, edge singularities and excitons in core level spectroscopy investigated within the dynamical mean-field theory, Europhys. Lett. **108**, 57004 (2014).

[38] Y. Lu, M. Höppner, O. Gunnarsson, and M. W. Haverkort, Efficient real-frequency solver for dynamical mean-field theory, Phys. Rev. B **90**, 085102 (2014).

[39] QUANTY version 0.81, https://www.quanty.org.

[40] Parameter set: $U_{dd} = 6.5$ eV, $U_{pd} = 8.2$ eV, charge transfer energy $\Delta = 6.5$ eV, SOC = 0.066 eV, ionic crystal field 10Dq(ion) = 0.45 eV, hybridization $V(e_g) = 1.59$ eV, $V(t_{2g}) = 0.67$ eV, ligand crystal field = 0.8 eV. Slater integrals reduced to 70% of Hartree-Fock values.

[41] O. Gunnarsson, O. K. Andersen, O. Jepsen, and J. Zaanen, in *Core-Level Spectroscopy in Condensed Systems* (Springer, Berlin, Heidelberg, 1988), pp. 82–98.

[42] S. P. Cramer, F. M. F. DeGroot, Y. Ma, C. T. Chen, F. Sette, C. A. Kipke, D. M. Eichhorn, M. K. Chan, W. H. Armstrong, E. Libby, G. Christou, S. Brooker, V. McKee, O. C. Mullins, and J. C. Fuggle, Ligand field strengths and oxidation states from manganese *L*-edge spectroscopy, J. Am. Chem. Soc. **113**, 7937 (1991).

[43] R. P. Wang, B. Liu, R. J. Green, M. U. Delgado-Jaime, M. Ghiasi, T. Schmitt, M. M. van Schooneveld, and F. M. F. de Groot, Charge-transfer analysis of 2*p*3*d* resonant inelastic x-ray scattering of cobalt sulfide and halides, J. Phys. Chem. C **121**, 24919 (2017).

[44] L. Kronik, Surface photovoltage phenomena: Theory, experiment, and applications, Surf. Sci. Rep. **37**, 1 (1999).

[45] T. Dittrich and S. Fengler, Surface photovoltage spectroscopy of ultrawide bandgap materials, Phys. Status Solidi Rapid Res. Lett. **19**, 2400384 (2025).

[46] A. Suzuki and T. Oku, Effects of transition metals incorporated into perovskite crystals on the electronic structures and magnetic properties by first-principles calculation, Heliyon **4**, e00755 (2018).

[47] C. Deluque-Toro, A. Gil-Rebaza, J. Villa-Hernández, D. Landínez-Téllez, and J. Roa-Rojas, Half-metallic electronic feature and thermophysical properties of the Ba_2CoMoO_6 perovskite-like cobalt molybdate, Rev. UIS Ing. **19**, 213 (2020).

[48] C. E. Deluque Toro, V. E. Vergara, A. V. Gil Rebaza, D. A. Landínez Téllez, and J. Roa-Rojas, Ground state structural, lattice dynamic, thermodynamic and optical properties of the Ba_2CaMoO_6 ordered perovskite, Physica B **666**, 415132 (2023).

[49] M. Ait Haddouch, A. Abbassi, Y. Aharbil, H. Labrim, Y. Tamraoui, F. Mirinioui, A. Benyoussef, L. Laânab, and S. Benmokhtar, Structural, electronic and optical properties of double perovskite oxide $BaSrMgTeO_6$, J. Appl. Surf. Interfaces **1**, 1 (2017).

[50] M. Nabi, S. S. Padelkar, J. J. Jasieniak, A. N. Simonov, and A. Alam, Lead-free magnetic double perovskites for photovoltaic and photocatalysis applications, Phys. Rev. Appl. **21**, 014063 (2024).

[51] S. Bazrafshan, J. He, and S. S. Naghavi, Charting Ba-based double perovskite oxides for visible-light-driven photocatalytic water splitting, J. Phys. Chem. C **127**, 3968 (2023).

[52] Z. Ghorbani and M. H. Ehsani, Photocatalytic activity and magnetic properties of Ba_2FeMoO_6 ferromagnetic double perovskite, Heliyon **10**, e29792 (2024).

[53] G. A. Bain and J. F. Berry, Diamagnetic corrections and Pascal's constants, J. Chem. Educ. **85**, 532 (2008).

[54] N. Fairley, V. Fernandez, M. Richard-Plouet, C. Guillot-Deudon, J. Walton, E. Smith, D. Flahaut, M. Greiner, M. Biesinger, S. Tougaard, D. Morgan, and J. Baltrusaitis, Systematic and collaborative approach to problem solving using x-ray photoelectron spectroscopy, Appl. Surf. Sci. Adv. **5**, 100112 (2021).

[55] G. Greczynski, Binding energy referencing in x-ray photoelectron spectroscopy: Expanded data set confirms that adventitious carbon aligns to the sample vacuum level, Appl. Surf. Sci. **670**, 160666 (2024).

[56] P. F. Liu, S. Yang, L. R. Zheng, B. Zhang, and H. G. Yang, Mo^{6+} activated multimetal oxygen-evolving catalysts, Chem. Sci. **8**, 3484 (2017).

[57] J. G. Choi and L. T. Thompson, XPS study of as-prepared and reduced molybdenum oxides, Appl. Surf. Sci. **93**, 143 (1996).